AIAA JOURNAL
Vol. 41, No. 2, February 2003

Experimental and Theoretical Study on Rolling Effectiveness of Multiple Control Surfaces

Deman Tang,* Aiqin Li,† and Earl H. Dowell‡
Duke University, Durham, North Carolina 27708-0300

It is well known that the effectiveness of a trailing-edge control surface can be substantially diminished due to the elastic twist of an airfoil or rolling wing. This aeroelastic phenomenon is known as control surface reversal when the lift or rolling rate vanishes at a sufficiently large ratio of flow dynamic pressure to airfoil or wing stiffness. However, a leading-edge control surface can be used to counteract control surface reversal, and, indeed, in principle, a leading-edge control surface can entirely cancel the tendency of the trailing-edge control surface to undergo reversal. Moreover, analysis shows that by using a simple adaptive control strategy, one can use a combination positive and negative control surface rotations to maximize lift and rolling effectiveness or minimize control surface rotations. In the present work, a theoretical–experimental study of the effectiveness of trailing- and leading-edge control surfaces has been made for a rolling wing–fuselage model. An experimental model and wind-tunnel test are used to assess the theoretical results. The theoretical model includes the inherently nonlinear dry friction damping moment between the spindle support and the experimental aeroelastic wing model for the rolling degree of freedom. A three-dimensional vortex lattice aerodynamic theory is employed. New insights into the behavior and design of an adaptive aeroelastic wing using trailing- and leading-edge control surfaces are provided.

Nomenclature

c	=	wing chord length
K_α	=	torsional stiffness
k_m, k_n	=	numbers of vortex elements on the wing in x and y directions, respectively
k_{mm}	=	total number of vortices on both the wing and wake in the x direction
L	=	total lift on the wing
L_{local}	=	local lift along the span
l	=	span length
M_d	=	Coulomb friction damping moment
p	=	wing rolling rate; aerodynamic pressure
R_a	=	size of reduced-order aerodynamic model
r_f	=	radius of the slender body
T_l, T_t	=	transfer matrices between the global and local vortex lattice mesh on leading and trailing control surfaces
T_p, T_α	=	rolling rate and elastic twist transfer matrices between the global and local vortex lattice mesh on the wing
t	=	time
U	=	airspeed
X_{Ra}, Y_{Ra}	=	reduced right and left eigenvector matrices of vortex lattice eigenvalue model
x, y	=	streamwise and spanwise coordinates
x_e	=	distance from the elastic center to leading edge of the wing
Z_{Ra}	=	reduced eigenvalue matrix of vortex lattice aerodynamic model
α	=	twist angle of the wing; relaxation factor
Γ	=	vortex strength
γ	=	reduced vortex strength
Δp	=	pressure distribution on the wing
Δt	=	time step, $\Delta x/U$
Δx	=	wing element length in the streamwise direction
η_{le}, η_{te}	=	rotational angles of the leading and trailing control surfaces
ρ_∞	=	air density
τ	=	nondimensional time, $\tau = tU/c$

Received 15 July 2001; revision received 30 July 2002; accepted for publication 19 September 2002.

*Research Associate Professor, Department of Mechanical Engineering and Materials Science. Member AIAA.

†Research Assistant, Department of Mechanical Engineering and Materials Science.

‡J. A. Jones Professor, Department of Mechanical Engineering and Materials Science; Director, Center for Nonlinear and Complex Systems; and Dean Emeritus, Pratt School of Engineering. Fellow AIAA.

Introduction

CONTROL surface reversal due to unfavorable aeroelastic effects is one of the classical phenomena of static aeroelasticity. It is treated in textbooks[1,2] and standard courses on aeroelasticity. However, an appropriately chosen combination of leading- and trailing-edge control surface deflections plus an adaptive control law can be used to achieve improved rolling performance and/or to minimize roll maneuver loads.

Related results have been reported from the Active Flexible Wing (AFW) program and more recent work on the Active Aeroelastic Wing (AAW) technology. Noll and Eastep[3] present a cogent overview and organized an issue of the *Journal of Aircraft* on the AFW program. In this special issue there are 11 papers that report theoretical and experimental investigations on actively controlled wings.

Anderson et al.[4] gave deeper insights into the favorable synergy that can be created by a combination of leading- and trailing-edge controls. In their work, they noted that the unfavorable aeroelastic twist that can lead to trailing-edge control surface reversal can be offset by a leading-edge control surface. Moreover, the trailing-edge control surface reversal can be eliminated and a constant roll authority maintained over a wide range of flight dynamic pressures by an appropriate combination of leading- and trailing-edge control surface deflections.

More recent work on the AAW technology has dealt with improvements in design optimization methodologies, reduction of drag, and an adaptive change in torsional stiffness to allow both pre- and postclassical reversal operation of an AAW.[5–8]

As reported previously,[9] the same conceptual benefit that can be obtained by using an adaptive torsional stiffness change can also be realized by using an AAW with the gearing ratio between leading- and trailing-edge control surfaces programmed to change with flight dynamic pressure. Also, some new actuation technologies are currently under development for high-bandwidth actuator, leveraging

high-energy density materials such as piezoceramics. Two such actuation technologies include the X-frame actuator developed at the Massachusetts Institute of Technology (MIT)[10] and the V-stack actuator developed at Duke University.[11] Thus, implementation of an AAW with leading- and trailing-edge control surfaces appears promising and practical.

The basic adaptive concept and the fundamental physical phenomena for two models of 1) an airfoil and 2) a rolling wing were considered in Ref. 9. These results using simple structural models and aerodynamic strip theory have shown the effectiveness of an adaptive strategy that programs the leading- and trailing-edge control surface rotations with flight condition. To validate the predictions of the theory, a wind-tunnel wing–fuselage model with the leading- and trailing-edge control surfaces has been designed and tested to measure the rolling effectiveness vs dynamic pressure for different combinations of leading- and trailing-edge control surface rotation. Of course, the wing–fuselage model is in a three-dimensional flowfield. A three-dimensional incompressible (linear) vortex lattice aerodynamic theory and a corresponding reduced-order aerodynamic model are used in the present analysis.[12] Results for subsonic, compressible flow can be obtained using the Prandtl–Glauert scaling law.

Finally, note that for the present wind-tunnel test model, there is a nonlinear dry friction damping arising from the rubbing or sliding between the experimental aeroelastic wing–fuselage model and the support spindle. This nonlinear factor is considered in the present experimental–theoretical study.

Experimental Model and Measurements

The experimental model consists of a right and left wing and a fuselage (slender body). For simplicity, the wing model is a rectangular aluminum plate of thickness 0.317 cm, total chord length c of 10.16 cm (including the leading and trailing control surface chords) and span length l of 10.16 cm. The plate has a very large bending and torsional stiffness, and, thus, the wing per se is assumed to be rigid. The leading and trailing control surfaces each have a chord length of 1.73 cm (17%c) and a full span length of 10.16 cm (100%l) hinged on the leading and trailing edges, respectively. The rotation angle of the control surface can be adjusted. The torsional flexibility of the wing is provided by a flat spring at the wing root, which can be adjusted. The elastic axis is placed at one-quarter of the wing chord. To also place the chordwise center of gravity axis of the wing at the elastic axis, the leading-edge control surface is made of brass, and the trailing control surface is made of aluminum plate. Also, a small slender body mounted at the wing root is used to provide weight balance.

The fuselage has a circular cross section with a diameter of 2.54 cm. It includes two parts. The front part is a slender body with a parabolic forebody that can rotate about the fuselage center axis and supports the wings. The rear part is a nonrotating slender body with a parabolic aftbody that is used to support the front portion of the slender body and is connected to the wind-tunnel floor by a support or sting rod (Fig. 1).

The wings are allowed to rotate (roll) about the center axis of the fuselage. The rolling rate (angular velocity) is measured by an angular transducer, R30A, mounted on the rear end of the nonrotating portion of the slender body.

A physical representation of wing model geometry along with a three-dimensional vortex lattice model (linear) of the unsteady flow is shown in Fig. 1, and a photograph of the aeroelastic model in the wind tunnel is shown in Fig. 2.

Static Aeroelastic Equations

As shown in Fig. 1, a straight rectangular wing with leading- and trailing-edge control surfaces that are full span is considered. The experimental model is symmetrical about the center axis of the fuselage. The aerodynamic forces on the fuselage (slender body) are neglected. The equation of torsional equilibrium about the elastic axis of the rigid wing is as follows.[1,2] It expresses the balance of moments about the elastic axis due to the elastic spring and the aerodynamic forces in the Eulerian coordinate system (x, y, z):

$$K_\alpha \alpha + M_y = 0 \tag{1}$$

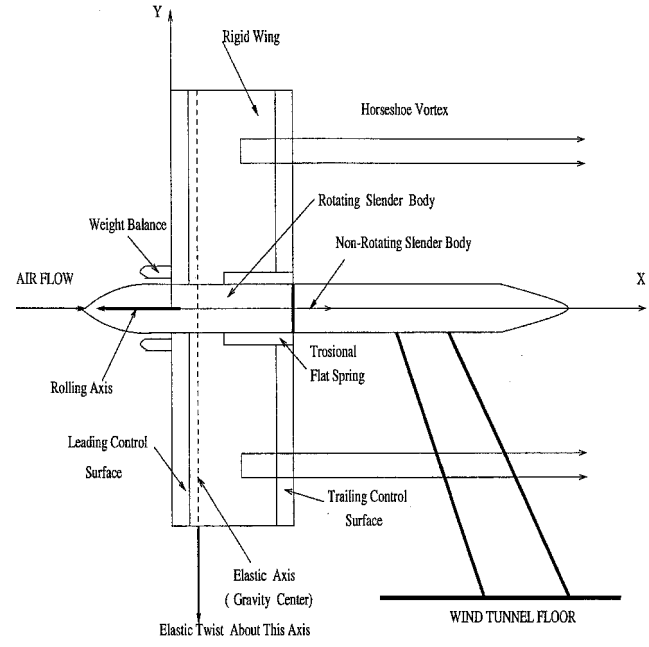

Fig. 1 Physical representation of experimental model; also shown is a three-dimensional vortex lattice model (linear) of the unsteady flow.

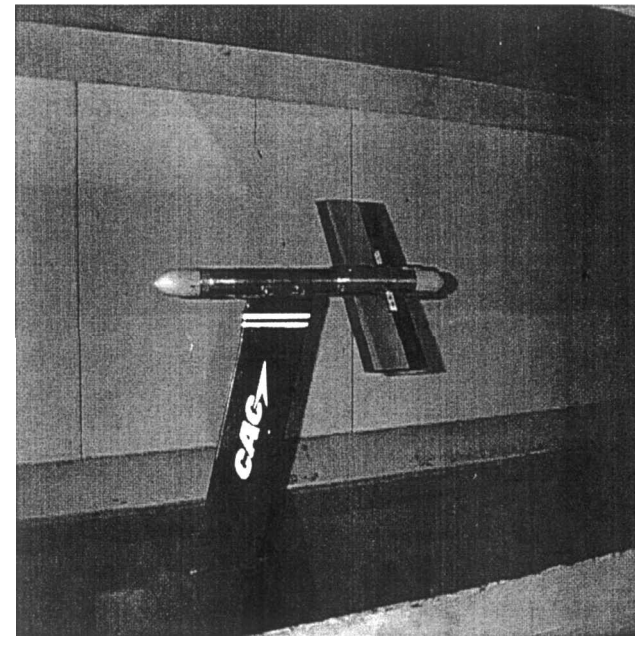

Fig. 2 Photograph of the aeroelastic model in the wind tunnel.

or

$$K_\alpha \alpha + \int_{r_f}^{l+r_f} \int_0^c \Delta p(x, y)(x - x_e)\, dx\, dy = 0 \tag{2}$$

where $\Delta p(x, y)$ is the pressure distribution on the wing, α is the twist angle of the wing, and r_f is the radius of the slender body (fuselage).

The rigid-body rolling equation of equilibrium about the center axis of the fuselage is expressed as follows:

$$\int_{r_f}^{l+r_f} Ly\, dy - M_d \frac{p}{|p|} = 0 \tag{3}$$

or

$$\int_{r_f}^{l+r_f} y \int_0^c \Delta p(x, y)\, dx\, dy - M_d \frac{p}{|p|} = 0 \tag{4}$$

In this equation, a dry friction damping moment between the spindle support and the aeroelastic wing model is taken into account. M_d is nonlinear and p is the wing rolling rate.

When nondimensional quantities in Eq. (2) and (4) are introduced as follows:

$$\overline{\Delta p}(x, y) = \Delta p(x, y)/\rho U^2, \qquad \bar{x} = x/c, \qquad \bar{x}_e = x_e/c$$

$$\bar{y} = y/c, \qquad \bar{K}_\alpha = K_\alpha \big/ \rho U^2 c^3, \qquad \bar{M}_d = M_d \big/ \rho U^2 c^3$$

the dimensionless equations corresponding to Eq. (2) and (4) are

$$\bar{K}_\alpha \alpha + \int_{r_f/c}^{(l+r_f)/c} \int_0^1 \overline{\Delta p}(\bar{x}, \bar{y})(\bar{x} - \bar{x}_e)\, \mathrm{d}\bar{x}\, \mathrm{d}\bar{y} = 0 \tag{5}$$

$$\int_{r_f/c}^{(l+r_f)/c} \bar{y} \int_0^1 \overline{\Delta p}(\bar{x}, \bar{y})\, \mathrm{d}\bar{x}\, \mathrm{d}\bar{y} - \bar{M}_d \frac{p}{|p|} = 0 \tag{6}$$

To model the preceding aeroelastic structural/fluid system, the aerodynamic flow about the structural model is assumed to be incompressible, inviscid, and irrotational. Here, an unsteady (linear) vortex lattice method is used to model this flow.[12] The wing and wake are divided into a number of elements. In the wake and on the wing, all of the elements are of equal size, $\mathrm{d}x$, in the streamwise direction. Point vortices are placed on the wing and in the wake at the quarter-chord of the elements. At the three-quarter chord of each panel element, a collocation point is placed for the downwash, that is, we require the velocity induced by the discrete vortices to equal the downwash arising from the unsteady motion of the wing. Thus, the following relationship is obtained:

$$w_i^{t+1} = \sum_j^{k_{mm}} K_{ij} \Gamma_j^{t+1}, \qquad i = 1, \ldots, k_m \tag{7}$$

where w_i^{t+1} is the dimensionless downwash at the ith collocation point at time step $t+1$, Γ_j is the jth normalized vortex strength by cU, and K_{ij} is an aerodynamic kernel function for the horseshoe vortex. For the three-dimensional incompressible flow, the kernel function is given by[13]

$$K_{ij}(\bar{x}, \bar{y}, \bar{x}_a, \bar{y}_a, \bar{x}_b, \bar{y}_b) = \frac{-1}{4\pi(\bar{y}_i - \bar{y}_{ja})}\left[1 + \frac{\sqrt{(\bar{x}_i - \bar{x}_{ja})^2 (\bar{y}_i - \bar{y}_{ja})^2}}{\bar{x}_i - \bar{x}_{ja}}\right] + \frac{1}{4\pi(\bar{y}_i - \bar{y}_{jb})}\left[1 + \frac{\sqrt{(\bar{x}_i - \bar{x}_{ja})^2 + (\bar{y}_i - \bar{y}_{jb})^2}}{\bar{x}_i - \bar{x}_{ja}}\right] \tag{8}$$

where $\bar{x}_i$ is the location of the ith collocation point, and $\bar{y}_{ja}$ and $\bar{y}_{jb}$ are the locations of the two jth trailing vortex segments that are parallel to the x axis at $\bar{y} = \bar{y}_a$ and $\bar{y} = \bar{y}_b$.

The aerodynamic matrix equation (general) is given by

$$[A]\{\Gamma\}^{t+1} + [B]\{\Gamma\}^t = [T]\{w\}^{t+1} \tag{9}$$

where $[A]$ and $[B]$ are aerodynamic coefficient matrices. $[T]$ is a transfer matrix for determining the relationship between the global vortex lattice mesh and the local vortex lattice mesh on the wing. For the present model, the wingspan is finite and antisymmetric about the center axis of the fuselage. An antisymmetric vortex condition is used for reducing the aerodynamic degrees of freedom. In this case, the aerodynamic coefficient matrix $[A]$, corresponding to the kernel function, can be expressed as

$$A = K_{i,j}(\bar{x}, \bar{y}, \bar{x}_a, \bar{y}_a, \bar{x}_b, \bar{y}_b) - K_{i,j}(\bar{x}, \bar{y}, \bar{x}_b, -\bar{y}_b, \bar{x}_a, -\bar{y}_a)$$

The nondimensional downwash w contains contributions from the twist angle of the wing α, the wing rolling rate p, and rotational angles, η_{le} and η_{te}, of the leading and trailing control surfaces, respectively. For the present model, Eq. (9) is expressed in matrix form as

$$[A]\{\Gamma\}^{t+1} + [B]\{\Gamma\}^t = \{T_\alpha\}\alpha^{t+1} - \{T_p\}(p^{t+1}/U) + \{T_t\}\eta_{\mathrm{te}} + \{T_l\}\eta_{\mathrm{le}} \tag{10}$$

where $\{T_\alpha\}$ and $\{T_p\}$ are the elastic twist and rolling rate transfer matrices for determining the relationship between the global vortex lattice mesh and the local vortex lattice mesh on the wing. $\{T_t\}$ and $\{T_l\}$ are the transfer matrices for determining the relationship between the global vortex lattice mesh and the local vortex lattice mesh on the trailing and leading control surfaces, respectively.

The nondimensional pressure distribution on the rigid wing at the jth point is given by

$$\overline{\Delta p_j} = \frac{c}{\Delta x}\left[\frac{\Gamma_j^{t+1} + \Gamma_j^t}{2} + \sum_i^j \left(\Gamma_i^{t+1} - \Gamma_i^t\right)\right] \tag{11}$$

Substituting Eq. (11) into Eq. (5) gives

$$\bar{K}_\alpha \alpha + \sum_{n=1}^{k_n}\sum_{m=1}^{k_m}(\bar{x}_m - \bar{x}_e) \times \left[\frac{\Gamma_{nm}^{t+1} + \Gamma_{nm}^t}{2} + \sum_i^m \left(\Gamma_{ni}^{t+1} - \Gamma_{ni}^t\right)\right]\Delta\bar{y} = 0 \tag{12}$$

or, as expressed in matrix form,

$$\bar{K}_\alpha \alpha + \{D_2\}^T\{\Gamma\}^{t+1} + \{D_1\}^T\{\Gamma\}^t = 0 \tag{13}$$

where k_n and k_m are the chordwise and spanwise numbers of vortex elements on the wing and, here, the superscript T indicates the matrix transpose.

Substituting Eq. (11) into Eq. (6) gives

$$\left\{\sum_{n=1}^{k_n}\bar{y}_n\sum_{m=1}^{k_m}\left[\frac{\Gamma_{nm}^{t+1} + \Gamma_{nm}^t}{2} + \sum_i^m \left(\Gamma_{ni}^{t+1} - \Gamma_{ni}^t\right)\right]\right\} \times \Delta\bar{y} - \bar{M}_d\frac{p}{|p|} = 0 \tag{14}$$

or, as expressed in matrix form,

$$\{C_2\}^T\{\Gamma\}^{t+1} + \{C_1\}^T\{\Gamma\}^t - \bar{M}_d(p/|p|) = 0 \tag{15}$$

where D_1, D_2, C_1, and C_2 are coefficient matrices describing the vortex element forces and moments on the wing.

Thus, when Eqs. (10), (13), and (15) are combined, a complete aeroelastic state-space equation in matrix form is obtained for the unknown variables Γ, α, and p:

$$\begin{bmatrix} A & -T_\alpha & T_p/U \\ D_2^T & \bar{K}_\alpha & 0 \\ C_2^T & 0 & 0 \end{bmatrix}\begin{Bmatrix}\Gamma \\ \alpha \\ p\end{Bmatrix}^{t+1} + \begin{bmatrix} B & 0 & 0 \\ D_1^T & 0 & 0 \\ C_1^T & 0 & 0 \end{bmatrix}\begin{Bmatrix}\Gamma \\ \alpha \\ p\end{Bmatrix}^t = \begin{Bmatrix} T_t\eta_{\mathrm{te}} + T_l\eta_{\mathrm{le}} \\ 0 \\ \bar{M}_d(p/|p|)\end{Bmatrix}^{t+\frac{1}{2}} \tag{16}$$

When a treatment similar to that described in Ref. 14 is followed, a reduced-order aerodynamic model with static correction is constructed, and the final aeroelastic state-space model is given by

$$\begin{bmatrix} I & -Y_{Ra}^T[I - A(A+B)^{-1}]E \\ G_2X_{Ra} & K + G_2(A+B)^{-1}E \end{bmatrix}\begin{Bmatrix}\gamma \\ \theta\end{Bmatrix}^{t+1} + \begin{bmatrix} -Z_{Ra} & Y_{Ra}^T B(A+B)^{-1}E \\ G_1X_{Ra} & G_1(A+B)^{-1}E \end{bmatrix}\begin{Bmatrix}\gamma \\ \theta\end{Bmatrix}^t = \begin{Bmatrix} 0 \\ -(G_1+G_2)(A+B)^{-1}(T_t\eta_{\mathrm{te}} + T_l\eta_{\mathrm{le}}) + F_N\end{Bmatrix}^{t+\frac{1}{2}} \tag{17}$$

where $\{\theta\} = \{\alpha,\ p\}$ is a vector of unknown variables and

$$[E] = [\{T_\alpha\}, \{-T_p/U\}], \qquad [G_2] = \begin{bmatrix} \{D_2\}^T \\ \{C_2\}^T \end{bmatrix}$$

$$[G_1] = \begin{bmatrix} \{D_1\}^T \\ \{C_1\}^T \end{bmatrix}, \qquad [K] = \begin{bmatrix} \bar{K}_\alpha & 0 \\ 0 & 0 \end{bmatrix}$$

$$\{F_N\} = \begin{Bmatrix} 0 \\ \bar{M}_d(p/|p|) \end{Bmatrix} \tag{18}$$

$[X_{Ra}]$ and $[Y_{Ra}]$ are the reduced right and left eigenvector matrices of the vortex lattice eigenvalue model and $[Z_{Ra}]$ is a reduced eigenvalue matrix, $\Gamma = X_{Ra}\gamma$, with only the most dominant eigenmodes retained in the analysis. Aerodynamic modes are retained on the basis of their damping values (real part of the aerodynamic eigenvalue) starting with the lowest damped aerodynamic mode. A convergence study is carried out by systematically increasing the number of aerodynamic modes retained.

Numerical Study

Validation of Aerodynamic Computation Code

To validate the present aerodynamic code, first consider a two-dimensional thin airfoil, and use two-dimensional vortex lattice theory at $M = 0$. Results are presented for the pressure and lift coefficient responses to a step angle of attack of the airfoil, leading and trailing control surfaces, that is, $\alpha = 1$ rad, $\eta_{le} = 1$ rad, and $\eta_{te} = 1$ rad, respectively. Control surface chords of 20% are considered. The airfoil was modeled using 40 vortex elements, that is, $k_m = 40$. The wake was modeled using 160 vortex elements, that is, $k_{mm} = 200$. The total number of vortex elements (or aerodynamic degrees of freedom) was 200. The vortex relaxation factor was taken to be $\alpha = 0.992$. The nonlinear Coulomb dry friction moment M_d is set to zero.

Figure 3 shows the lift coefficient of the airfoil vs nondimensional time, $\tau(\tau = tU/c)$. The solid line is for $\alpha = 1$ rad, the broken line is for $\eta_{le} = 1$ rad, and the dashed line is for $\eta_{te} = 1$ rad step angle-of-attack excitations. Figure 4 shows the corresponding nondimensional pressure distributions vs nondimensional chord x as the flow reaches its steady state $\tau \to \infty$. A comparison between the present results and typical values of the aerodynamic coefficients from Ref. 15 is shown below in Table 1. The agreement is very close.

Consider now the present three-dimensional flow model for the wing. Here again, the aerodynamic coefficients are calculated. The wing was modeled using 400 vortex elements, that is, $k_m = 40$ and $k_n = 10$. The wake was modeled using 800 vortex elements, that is, $k_{mm} = 120$. The total number of vortex elements (or aerodynamic degrees of freedom) was 1200. The control surface chords are 20% of the total wing chord, and the spans are 50% of the total wingspan. The control surfaces are located on the outer half of the wingspan.

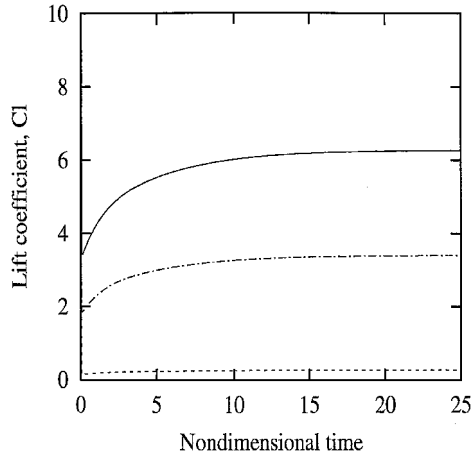

Fig. 3 Lift coefficients of a thin airfoil vs nondimensional time τ for several different step angle-of-attack excitations of the airfoil and control surfaces.

Table 1 Comparison between present results and typical values from Ref. 15

Coefficient	Ref. 15	Present method
$C_{M\,AC\alpha}$	0	−0.0037
$C_{M\,AC\eta_{te}}$	−0.64	−0.65
$C_{M\,AC\eta_{le}}$	0.16	0.165
$C_{L\alpha}$	2π	6.271
$C_{L\eta_{te}}$	3.45	3.398
$C_{L\eta_{le}}$	0.255	0.266

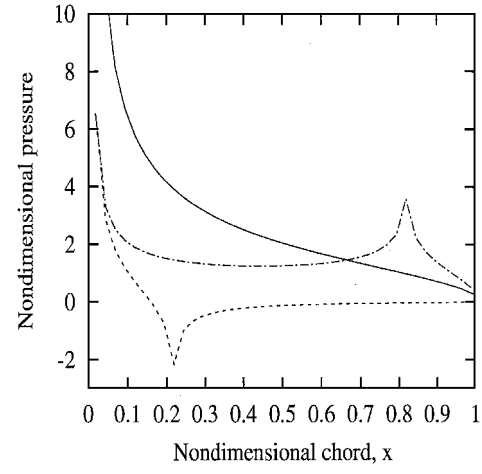

Fig. 4 Nondimensional pressure distribution of a thin airfoil vs nondimensional chord position for different step angle-of-attack excitation as $\tau \to \infty$.

Both local and total aerodynamic lift coefficients are considered. The nonlinear Coulomb dry friction moment M_d is set to zero.

The local lift at $y = y_j$ is obtained by integrating the pressure difference along the local chord line:

$$L^{t+1}_{\text{local}}(y_j) = \int_0^c \Delta p^{t+1}(x, y_j)\,\mathrm{d}x \tag{19}$$

The local lift coefficient $C_{l,\text{local}}$ at $y = y_j$ is defined as

$$C^{t+1}_{l,\text{local}}(y_j) = \frac{L^{t+1}_{\text{local}}(y_j)}{\frac{1}{2}\rho U^2 c} \tag{20}$$

The total lift is obtained by integrating the local total lift along the span:

$$L^{t+1} = \int_{r_f}^{l+r_f} L^{t+1}_{\text{local}}(y)\,\mathrm{d}y = l\sum_{j=1}^{k_n} L^{t+1}_{\text{local}}(y_j)\Delta\bar{y} \tag{21}$$

where $\Delta\bar{y} = (l/c)(1/k_n)$ and k_n is the number of spanwise discrete elements.

The total aerodynamic lift coefficient C_l is defined by

$$C^{t+1}_l = \frac{L^{t+1}}{\frac{1}{2}\rho U^2 A_w} \tag{22}$$

where A_w is the total wing area.

The results are shown in Figs. 5a and 5b for step angles of attack of the wing, leading, and trailing control surfaces, respectively. Figure 5a shows the total lift coefficient of the wing vs nondimensional time τ. The solid line is for $\alpha = 1$ rad, the dashed line is for $\eta_{le} = 1$ rad, and the broken line is for $\eta_{te} = 1$ rad step angle-of-attack excitations of the aerodynamic flow. All results have reached their steady values when $\tau > 10$. The steady total lift coefficients of the wing are $C_{L\alpha} = 1.97$, $C_{L\eta\,te} = 0.73$, and $C_{L\eta\,le} = 0.021$. Note that the lift contribution due to the leading-edge control surface is quite small relative to the wing and trailing-edge control surface. Figure 5b shows the corresponding nondimensional pressure distribution at midspan vs nondimensional wing chord as $\tau \to \infty$. For the step angle-of-attack excitation of the wing, the maximum pressure is near the leading edge. For the leading control surface, the

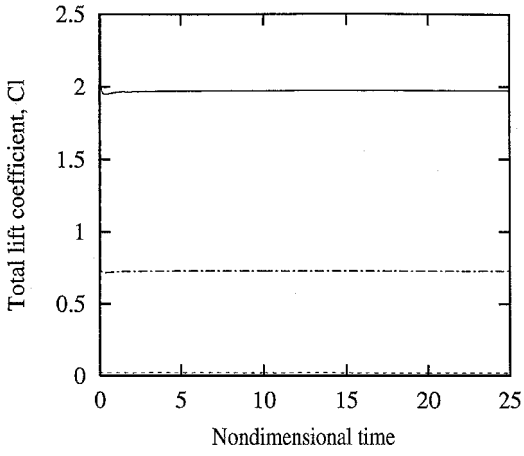

a)

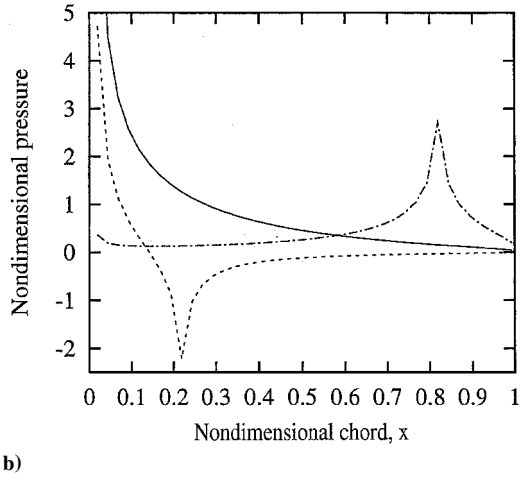

b)

Fig. 5 Aerodynamic response to step angles of attack for wing, leading-, and trailing-edge control surfaces: a) total lift coefficients and b) nondimensional pressure distribution ($\tau \to \infty$).

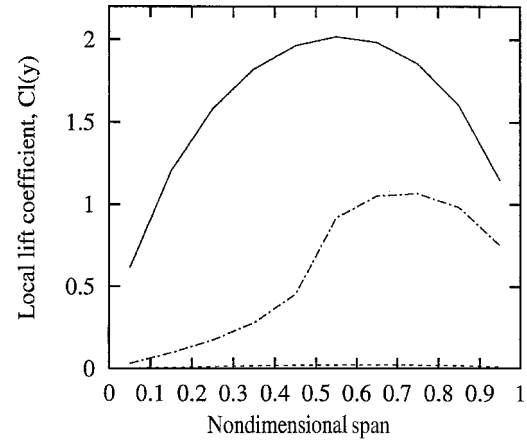

a)

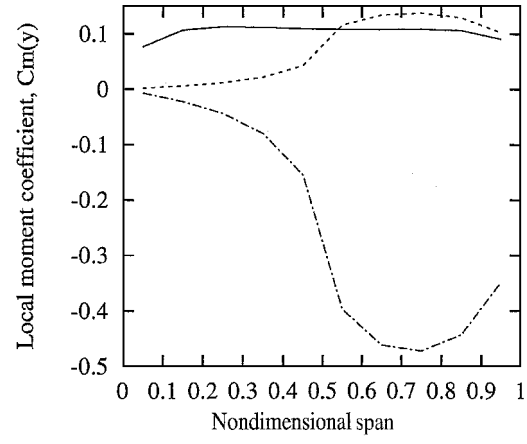

b)

Fig. 6 Aerodynamic response to step angles of attack for wing, leading-, and trailing-edge control surfaces: a) local lift coefficients and b) local moment coefficients along the span.

maximum pressure is still at the leading edge, but there is a negative peak pressure ($\overline{\Delta p} = -2.2$) at $\bar{x} = 0.22$, that is, near the trailing edge of the leading-edge control surface. The pressure distribution is almost zero when $\bar{x} > 0.3$. For the trailing-edge control surface, the maximum pressure is ($\overline{\Delta p} = 2.7$) at $\bar{x} = 0.82$, that is, near the leading edge of the trailing-edge control surface.

Figure 6a shows the local lift coefficient of the wing vs nondimensional span. As expected, the local lift coefficient decreases near the tip and root of the wing for the step angle-of-attack excitation of the wing. (Note that an antisymmetric vortex condition is used.) The maximum value of 2.06 at $\bar{y} = 0.55$ is about 30% of that for a thin airfoil. For the leading-edge control surface step angle-of-attack excitation, the maximum local lift coefficient is 0.024 at $\bar{y} = 0.65$. For the trailing-edge control surface step angle-of-attack excitation, the maximum local lift coefficient is 1.06 at $\bar{y} = 0.75$. Figure 6b shows the local moment coefficient of the wing vs nondimensional span. For the step angle-of-attack excitation of the wing, the maximum value is 0.11 at $\bar{y} = 0.25$. For the leading-edge control surface excitation, the maximum local moment coefficient is 0.14 at $\bar{y} = 0.75$. For the trailing-edge control surface excitation, the maximum local moment coefficient is -0.47 at $\bar{y} = 0.75$.

Figures 5 and 6 are the results for the right wing. For the left wing, the aerodynamic excitations and forces are antisymmetrical with respect to the center axis of the fuselage. Note that rolling is not permitted in this purely aerodynamic simulation.

Numerical Results for Effectiveness of Control Surfaces

A standard discrete time marching algorithm has been used to calculate the static response of this aeroelastic system using the full aerodynamic model, Eq. (16), and also the reduced-order aerodynamic model, Eq. (17). The time step is constant for a given flow velocity U, $\Delta t = \Delta x/U$. For these calculations, $\bar{x}_e = 0.3$, $K_\alpha = 0.131$ kgm/rad, and $M_d = 0$. The rotation angles of the leading and trailing control surfaces, η_{le} and η_{te}, are the variables for a given flow velocity.

For the following discussion, the nondimensional dynamic pressure λ, rolling effectiveness (RE) and rolling rate normalized by the trailing-edge control surface rotation $\tilde{P}$ are defined as

$$\lambda \equiv \rho U^2 c^3 \Big/ K_\alpha, \qquad \text{RE} \equiv (pl/U)/(pl/U)_{\text{rigid}}$$

$$\lambda_R \equiv \lambda \mid_{pl/u=0}$$

$$\tilde{P} \equiv \left(pl \Big/ \sqrt{K_\alpha / \rho c^3} \right) \Big/ \eta_{te} = \sqrt{\lambda}(pl/U)/\eta_{te} \qquad (23)$$

Figure 7 shows RE vs dynamic pressure λ for several different ratios of leading- to trailing-edge control surface rotation. Rolling reversal occurs, that is, $pl/U = 0$ when $\lambda = 1.1$, 0.6, 0.4, 0.3, 0.2, and 0.15 for $r = 3$, 2, 1, 0, -1, and -2, respectively. Note that λ_R decreases as r decreases. Figure 8 shows the twist angle α vs dynamic pressure. The twist angle increases as dynamic pressure increases and r decreases for the range of parameters shown.

Figure 9 shows the variation of rolling rate $\tilde{P}$ vs dynamic pressure λ for $r = 3, 2, 0$, and -2. In our linear aeroelastic model, the rolling rate is proportional to the trailing-edge rotation for a fixed ratio of leading- to trailing-edge rotations. Thus, the inverse of Fig. 9 may also be interpreted as the trailing-edge rotation required for a given rolling rate.

Note that to achieve the maximum rolling rate, one should reverse the sign of r near $\lambda = \lambda_R|_{r=0}$ as was found previously for simpler models.[9]

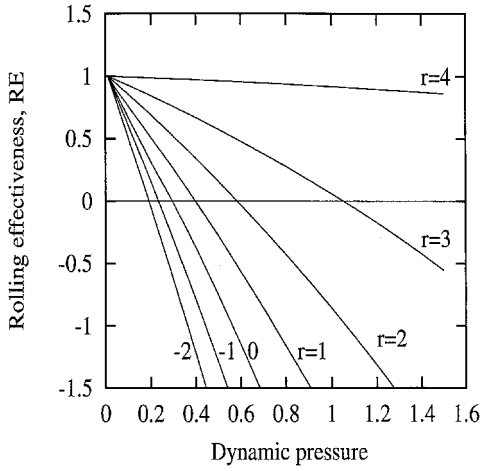

Fig. 7 RE vs dynamic pressure λ for different r.

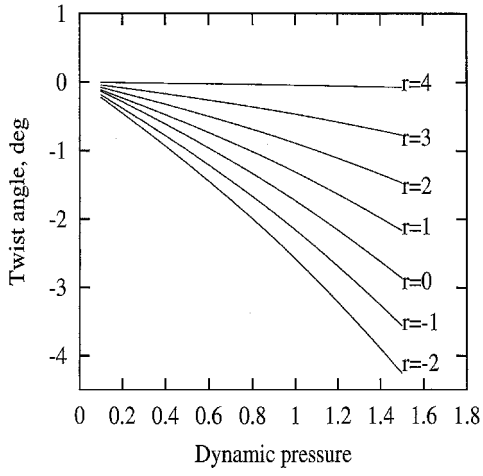

Fig. 8 Elastic twist angle α vs dynamic pressure λ for different r.

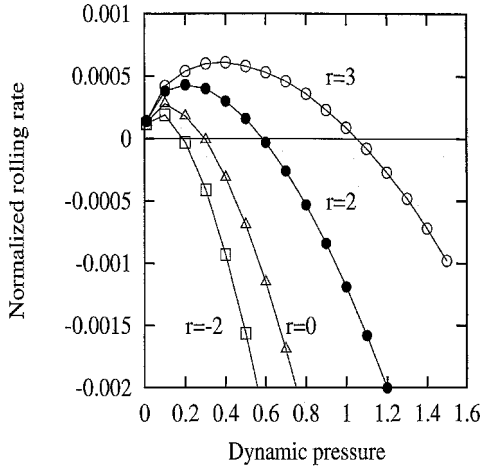

Fig. 9 Variation of normalized rolling rate $\tilde{P}$ vs dynamic pressure λ for $r = 3, 2, 0,$ and -2.

Theoretical and Experimental Correlation

For the present computational and experimental model, the aerodynamic and structural parameters are described in the preceding section, "Experimental Model and Measurements." The measured torsional stiffness is $K_\alpha = 0.032$ kg/rad. The trailing-edge control surface rotation is $\eta_t = 5$ deg. Three typical cases for leading-edge control are considered, that is, the ratios of leading- to trailing-edge control surface rotations are $r = -1$, 0, and 1.

The dry friction damping moment between the spindle support and the aeroelastic wing model M_d is determined by an experimental method, as follows. From the wind-tunnel test, a specific flow velocity called U_d can be determined where the rolling is just started from a rest state due to the aerodynamic rolling moment overcoming the dry friction moment in the test model. Note that this flow velocity varies with the structural paramenters. When the known U_d and $p = 0$ are substituted into Eqs. (10) and (13), the state variables, Γ^t, Γ^{t+1}, and α^{t+1} can be solved using a standard discrete algorithm. By the use of Eq. (15), the Coulomb friction moment M_d of this system can be determined by

$$\bar{M}_d = \{C_2\}^T\{\Gamma\}^{t+1} + \{C_1\}^T\{\Gamma\}^t \tag{24}$$

where

$$M_d = \bar{M}_d \rho U_d^2 c^3 \tag{25}$$

Note that $p/|p| \equiv 1$ when $p = 0$.

The Coulomb friction moment M_d obtained from the experiment has a small variation with r. An average value, $M_d = 0.00021$ kgm, is used in the following calculations.

Either Eq. (16) or Eq. (17) is a nonlinear equation to determine p and α when M_d is known. The computational procedure is follows.

When a set of initial values Γ^t, α^t, and $p^t = 0$ is assumed, the state variables of the next time step, $t + 1$, can be calculated using Eq. (16) or (17). Now, if

$$\left|\{C_2\}^T\{\Gamma\}^{t+1} + \{C_1\}^T\{\Gamma\}^t\right| \le \bar{M}_d$$

then $p = 0$; otherwise, the computational code is time marched using the preceding state as the set of initial conditions until the system achieves a steady state. Note that the transient time histories computed here are for very light (zero moment of inertia) wings, and, hence, they are not shown because they are of little physical interest. Later studies will incorporate realistic moments of inertia.

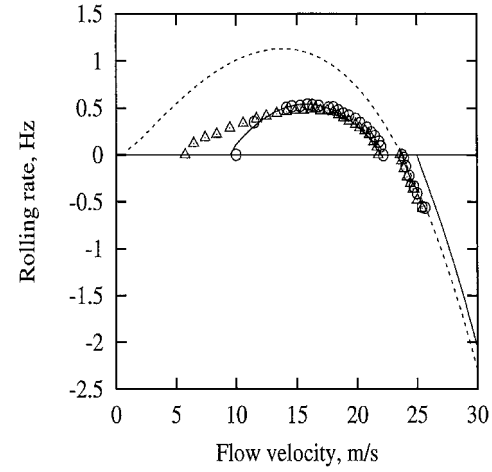

Fig. 10 Rolling rate vs flow velocity: comparison of theory and experiment for $r = 0$, and with flexible torsional stiffness.

Figure 10 shows the steady-state rolling rate vs flow velocity and a comparison of theory and experiment for a certain combination of leading- and trailing-edge control surface rotations, that is, zero leading-edge control surface rotation $r = 0$ and the flexible torsional stiffness case. Note that two theoretical results are shown, with (solid line) and without (broken line) the dry friction of the spindle support mechanism included. The symbols of $\triangle$ and $\circ$ points are results obtained from the experiment. The $\circ$ points show the results when flow velocity increases and the $\triangle$ points are for when flow velocity decreases. These two experimental results are very close, except for the flow velocity at which rolling starts when increasing flow velocity or stops when decreasing flow velocity. The starting flow velocity is about $U_d = 10.3$ m/s and the stopping flow velocity is about 5.4 m/s. This difference is because there is an inertial rolling moment when the flow velocity is decreasing and the wing is still rolling. From Fig. 10 it is seen that the theoretical reversal flow velocity is in a range from $U = 21.5 \rightarrow 25$ m/s for dry friction damping included and at a point velocity at $U = 23.6$ m/s for no dry friction damping included. The experimental reversal flow velocity is also

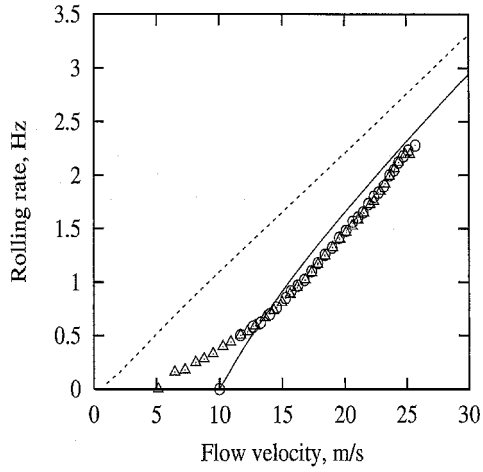

Fig. 11 Rolling rate vs flow velocity: comparison of theory and experiment for $r = 0$ and with rigid torsional stiffness.

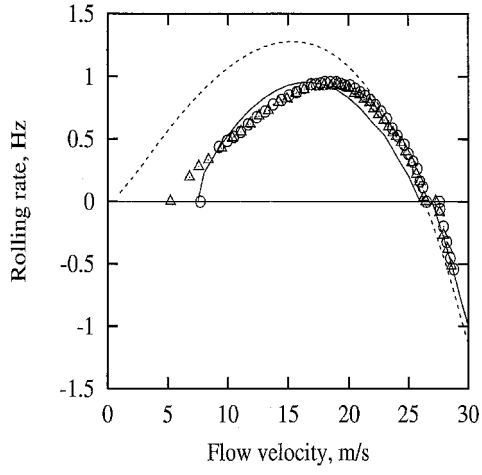

Fig. 12 Rolling rate vs flow velocity: comparison of theory and experiment for $r = 1$ and with flexible torsional stiffness.

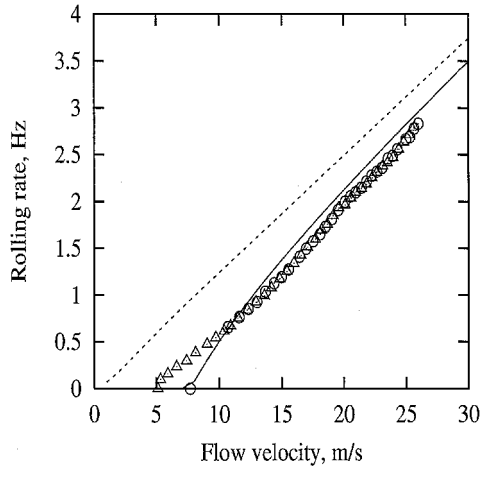

Fig. 13 Rolling rate vs flow velocity comparison of theory and experiment for $r = 1$ and with rigid torsional stiffness.

in a range from $U = 21.6 \rightarrow 24$ m/s for increasing flow velocity, and $U = 21.5 \rightarrow 23.7$ m/s for decreasing flow velocity.

Figure 11 shows the corresponding rolling rate vs flow velocity for the rigid torsional stiffness case. The lines and symbols shown in Fig. 11 are the same as for Fig. 10. Accounting for the dry friction improves the quantitative agreement between theory and experiment both for the rigid and flexible torsional stiffness cases.

Figure 12 shows the rolling rate vs flow velocity for $r = 1$ and the flexible torsional stiffness case. The experimental starting flow

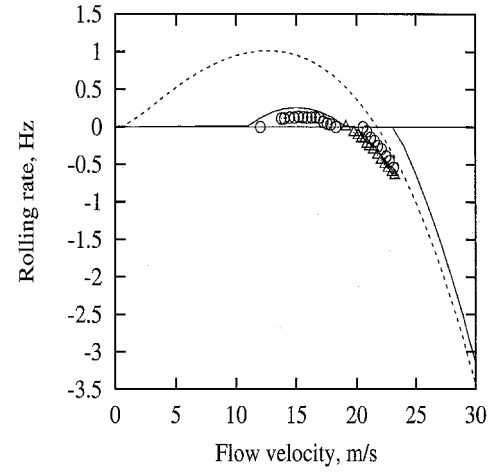

Fig. 14 Rolling rate vs flow velocity comparison of theory and experiment for $r = -1$ and with flexible torsional stiffness.

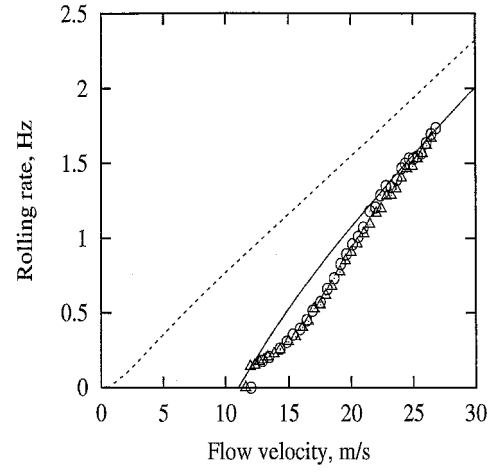

Fig. 15 Rolling rate vs flow velocity: comparison of theory and experiment for $r = -1$ and with rigid torsional stiffness.

velocity is about $U_d = 7.5$ m/s and the stopping flow velocity is about 5.2 m/s. From Fig. 12, it is also seen that the theoretical reversal flow velocity is in a range from $U = 25 \rightarrow 27$ m/s for dry friction damping included and at a point velocity at $U = 26.5$ m/s for no dry friction damping included. These are higher than those for the $r = 0$ case. The experimental reversal flow velocity is also in a range from $U = 26.5 \rightarrow 27.6$ m/s for both increasing and decreasing flow velocity. A similar result is shown in Fig. 13 for the rigid torsional stiffness case.

Figures 14 and 15 show the rolling rate vs flow velocity for $r = -1$ for the flexible and the rigid torsional stiffness cases, respectively. The experimental starting flow velocity is about $U_d = 12$ m/s. The theoretical reversal flow velocity is from $U = 19 \rightarrow 23$ m/s for dry friction damping included and at a point velocity at $U = 21.5$ m/s for no dry friction damping included. The experimental reversal flow velocity is from $U = 17.2 \rightarrow 21$ m/s for increasing flow velocity. The difference between the experimental data for increasing and decreasing flow velocity is larger for $r = -1$ than for $r = 0$ or $+1$ due to a smaller rolling rate, that is, there is a smaller aerodynamic rolling moment relative to the dry friction damping moment. For decreasing flow velocity, the stopping flow velocity is at 19.1 m/s. For the rigid torsional stiffness case, as shown in Fig. 15, the agreement between theory and experiment is closer because the aerodynamic rolling moment is more dominant relative to the dry friction damping moment.

To more clearly show the effects of the parameter r on the reversal flow velocity and rolling rate pl/U, a summary of data from Figs. 10–15 is shown in Figs. 16 and 17. Figure 16 shows the rolling rate vs flow velocity for $r = -1$, 0, and 1 and the flexible torsional stiffness case. Figure 17 shows the corresponding rolling rate vs

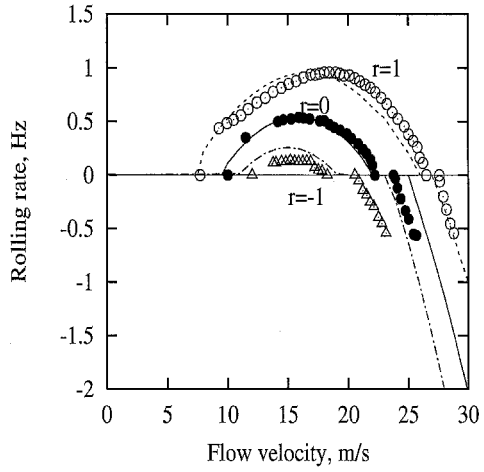

Fig. 16 Rolling rate vs flow velocity: comparison of theory and experiment for $r = -1$, 0, and 1 and with flexible torsional stiffness.

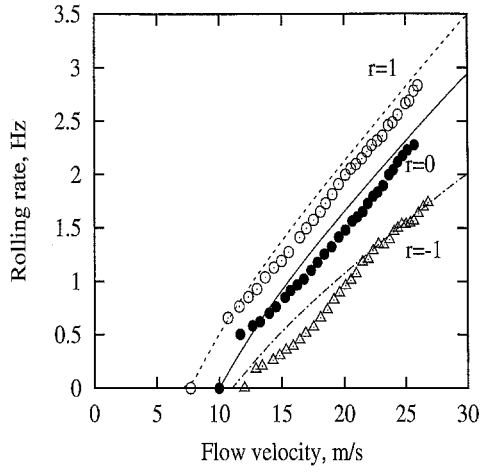

Fig. 17 Rolling rate vs flow velocity: comparison of theory and experiment for $r = -1$, 0, and 1 and with rigid torsional stiffness.

flow velocity for the rigid torsional stiffness case. When Fig. 16 is compared to Fig. 7 or Fig. 9, it is found the reversal flow velocity decreases as r decreases, both theoretically and experimentally.

Conclusions

The generally good agreement between theory and experiment is encouraging and perhaps even a bit of a pleasant surprise. It is encouraging because it confirms that the adaptive use of a combination of leading- and trailing-edge control surfaces can lead to substantially improved rolling performance in aerospacecraft and, by implication, enhanced performance for other maneuvers as well.

Note that, to obtain good quantitative agreement between theory and experiment, it was necessary to model the nonlinear dry friction damping at the interface between the wing experimental model and its support mounting. In a freely flying model, such dry friction would not be present, of course.

The good agreement between theory and experiment may also be a bit surprising for those who have been aware that often the prediction of aerodynamic characteristics of control surfaces has been found to be deficient relative to measured values. Although direct measurements of the aerodynamic characteristics of the leading- and trailing-edge control surfaces have not been made here, nevertheless, the very good agreement between theory and experiment for rolling rates as a function of dynamic pressure suggests that our theoretical aerodynamic model has been more than adequate to predict the aerodynamic performance of the control surfaces. This may be because, for the present experimental model, there is no gap between the wing and the control surfaces that would lead to leakage flows. On the other hand, viscous effects, per se, which are often cited as a possible source of disagreement between measured and computed values, must not be significant here, even though the Reynolds' number based on the total wing chord is only about 1.36×10^5 for $U = 20$ m/s.

Finally, with regard to possible next steps, even though we have used time marching simulation to compute the steady-state rolling performance, the present experimental/theoretical study is essentially for static equilibrium conditions. It will be of considerable interest to extend the theoretical and experimental work to dynamic, transient conditions.

Acknowledgments

This work was supported by the Defense Advanced Research Projects Agency through U.S. Air Force Office of Scientific Research Grant F49620-99-1-00253, "Aeroelastic Leveraging and Control Through Adaptive Structures," under the direction of Ephrahim Garcia and Dan Segalman. Robert Clark was the Duke University Principal Investigator. All numerical calculations were done on a supercomputer, T916, in the North Carolina Supercomputing Center.

References

[1]Bisplinghoff, R. L., Ashley, H., and Halfman, R. L., *Aeroelasticity*, Addison Wesley Longman, Reading, MA, 1955, pp. 421–526.

[2]Dowell, E. H., Crawley, E. F., Curtiss, H. C., Jr., Peters, D. A., Scanlan, R. H., and Sisto, F., *A Modern Course in Aeroelasticity*, 3rd ed., Kluwer, Dordrecht, The Netherlands, 1995.

[3]Noll, T. E., and Eastep, F. E., "Active Flexible Wing Program," *Journal of Aircraft*, Vol. 32, No. 1, 1995, p. 9.

[4]Andersen, G., Forster, E., Kolonay, R., and Eastep, F., "Multiple Control Surface Utilization in Active Aeroelastic Wing Technology," *Journal of Aircraft*, Vol. 34, No. 4, 1997, pp. 552–557.

[5]Zink, P. S., Mavris, D. N., Love, M. H., and Karpel, M., "Robust Design for Aeroelastically Tailored/Active Aeroelastic Wing," AIAA Paper 98-4781, Sept. 1998.

[6]Weisshaar, T. A., Duke, D. K., and Dobbins, A., "Active Aeroelastic Tailoring with Adaptive Continuous Control Surfaces," AIAA Paper 2000-1619, April 2000.

[7]Flick, P. M., and Love, M. H., "The Impact of Active Aeroelastic Wing Technology on Conceptual Aircraft Design," Research and Technology Organization, Rept. RTO MP-36, Oct. 1999.

[8]Yurkovich, R. R., "Optimum Wing Shape for an Active Flexible Wing," *Proceedings of the AIAA/ASME/ASCE/ARS 36th Structures, Structural Dynamics, and Materials Conference*, AIAA, Washington, DC, 1995, pp. 520–530.

[9]Dowell, E. H., Bliss, D. B., and Clark, R. L., "An Adaptive Aeroelastic Wing with Leading and Trailing Edge Control Surfaces," *Journal of Aircraft* (to be published).

[10]Prechtl, E. F., and Hall, S. R., "Design of a High-Efficiency, Large-Stroke, Electromechanical Actuator," *Journal of Smart Materials and Structures*, Vol. 8, No. 1, 1999, pp. 13–30.

[11]Ardilean, E., and Clark, R. L., "V-Stack Piezoelectric Actuator," *Proceedings of the Society of Photo-Optical Instrumentation Engineers, Smart Structures and Materials*, Vol. 4333, 2001, pp. 322–333.

[12]Dowell, E. H., and Hall, K. C., "Modeling of Fluid–Structure Interaction," *Annual Review of Fluid Mechanics*, Vol. 33, 2001, pp. 445–490.

[13]Katz, J., and Plotkin, A., *Low-Speed Aerodynamics*, McGraw–Hill, New York, 1991, p. 297.

[14]Tang, D. M., and Dowell, E. H., "Effects of Angle of Attack on Nonlinear Flutter of a Delta Wing," *AIAA Journal*, Vol. 39, No. 1, 2001, pp. 15–21.

[15]Kuethe, A. M., and Chow, C.-Y., *Foundations of Aerodynamics: Bases of Aerodynamic Design*, Wiley, New York, 1986.

E. Livne
Associate Editor